Characterization of noise amplifiers with global singular modes: the case of the leading-edge flat-plate boundary layer

Denis Sipp & Olivier Marquet

Theoretical and Computational Fluid Dynamics

ISSN 0935-4964
Volume 27
Number 5

Theor. Comput. Fluid Dyn. (2013)
27:617-635
DOI 10.1007/s00162-012-0265-y

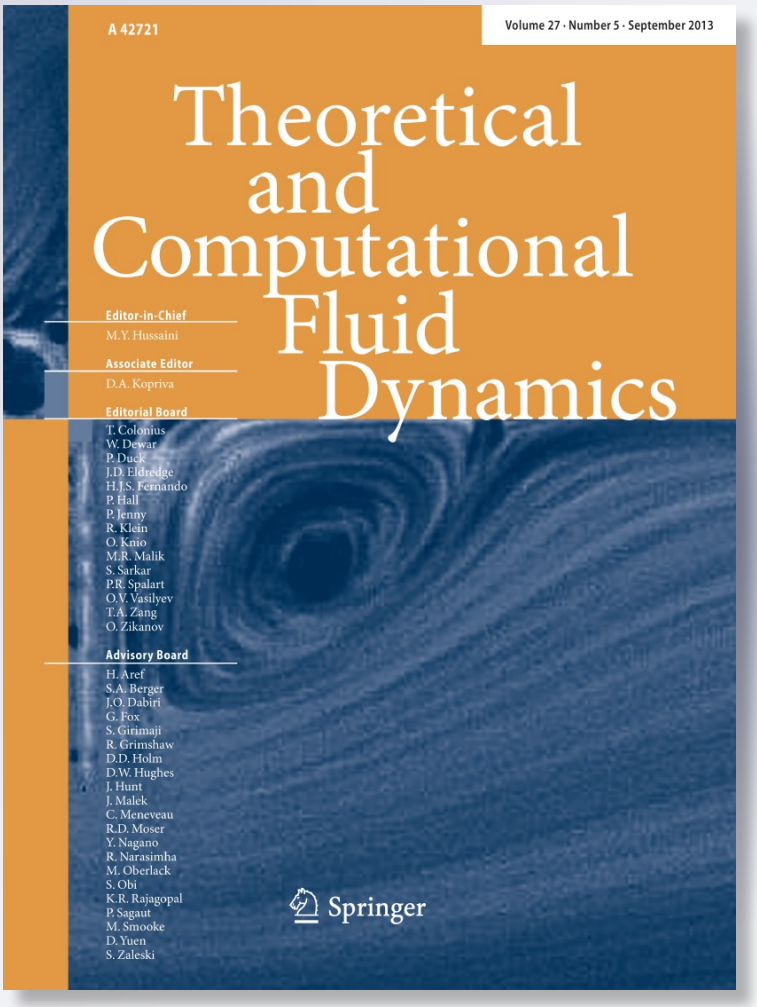

Springer

Theor. Comput. Fluid Dyn. (2013) 27:617–635
DOI 10.1007/s00162-012-0265-y

ORIGINAL ARTICLE

Denis Sipp · Olivier Marquet

Characterization of noise amplifiers with global singular modes: the case of the leading-edge flat-plate boundary layer

Received: 27 July 2011 / Accepted: 28 March 2012 / Published online: 11 April 2012

Abstract This article deals with the linear dynamics of a transitional boundary layer subject to two-dimensional Tollmien–Schlichting instabilities. We consider a flat plate including the leading edge, characterized by a Reynolds number based on the length of the plate equal to $Re = 6 \times 10^5$, inducing a displacement thickness-based Reynolds number of 1,332 at the end of the plate. The global linearized Navier–Stokes equations only display stable eigenvalues, and the associated eigen-vectors are known to poorly represent the dynamics of such open flows. Therefore, we resort to an input–output approach by considering the singular value decomposition of the global resolvent. We then obtain a series of singular values, an associated orthonormal basis representing the forcing (the so-called optimal forcings) as well as an orthonormal basis representing the response (the so-called optimal responses). The objective of this paper is to analyze these spatial structures and to closely relate their spatial downstream evolution to the Orr and Tollmien–Schlichting mechanisms. Analysis of the spatio-frequential diagrams shows that the optimal forcings and responses are respectively localized, for all frequencies, near the upstream neutral point (branch I) and the downstream neutral point (branch II). It is also shown that the spatial growth of the dominant optimal response favorably compares with the e^N method in regions where the dominant optimal forcing is small. Moreover, thanks to an energetic input–output approach, it is shown that this spatial growth is solely due to intrinsic amplifying mechanisms related to the Orr and Tollmien–Schlichting mechanisms, while the spatial growth due to the externally supplied power by the dominant optimal forcing is negligible even in regions where the dominant optimal forcing is strong. The energetic input–output approach also yields a general method to assess the strength of the instability in amplifier flows. It is based on a ratio comparing two quantities of same physical dimension, the mean-fluctuating kinetic energy flux of the dominant optimal response across some boundary and the supplied mean external power by the dominant optimal forcing. For the present boundary-layer flow, we have computed this amplification parameter for each frequency and discussed the results with respect to the Orr and Tollmien–Schlichting mechanisms.

Keywords Stability · Noise amplifier · Boundary layer

1 Introduction

According to Huerre et al. [1], unsteadiness in open flows can be classified into two main categories. The flow can behave as an *oscillator* and impose its own dynamics (intrinsic dynamics), or the flow can behave as a *noise amplifier* and reflect in some extent the noise already present in the upstream flow (extrinsic dynamics). For example, the cylinder flow characterized by a Reynolds number in the range $47 < Re < 180$ is typical of the family of oscillators, while a homogeneous jet or a Blasius boundary layer (viewed in a global setting)

Communicated by T. Colonius.

D. Sipp (✉) · O. Marquet
ONERA-The French Aerospace Lab, 8 rue des vertugadins, 92190 Meudon, France
E-mail: denis.sipp@onera.fr

is characteristic of the family of noise amplifiers. In a linear global framework, where both the stream-wise and cross-stream directions are solved for, these two classes of flows exhibit different characteristics of the global linearized Navier–Stokes (GLNS) operator. The oscillator flow corresponds to a globally unstable flow and displays at least one unstable global mode, that is, one unstable eigenvalue of the GLNS operator. In the case of the cylinder flow, Zebib [2], Jackson [3], Provansal et al. [4], and Sipp et al. [5] showed that the first bifurcation was linked to a Hopf bifurcation.

Amplifier flows, on the other hand, are globally stable in the sense that all eigenvalues of the GLNS operator are stable. Chomaz [6] and Marquet et al. [7] showed that the linearized Navier–Stokes equations are strongly non-normal in open flows due to the downstream advection of the perturbations and to the lift-up mechanism. Trefethen et al. [8] showed that this property may generate strong energy amplifications. These amplifications may be highlighted by an input–output analysis [9] carried out either in the temporal or in the frequency domain. In the former, the impulsive linear response of the flow is investigated by looking for optimal initial perturbations that maximize the energy of the perturbation at some given time T. In the latter, the long-time linear response of the flow to harmonic sustained forcing is investigated by looking for optimal forcings that maximize the energy of the flow response at some given frequency ω.

For open flows, most of the theoretical studies [10–13] have been performed in the temporal domain. The frequency-based approach is nevertheless attractive since external perturbations in open flow experiments are often described as upstream sustained disturbances characterized by a given spectrum. Frequency-based methods therefore play a central role in the characterization of low-order models. For example, the dynamic mode decomposition (DMD) [14] decomposes a temporal evolution into dynamic modes characterized by particular frequencies. Hence, to study noise amplifiers, we will look for optimal forcings and try to identify pseudo-resonances in the spectrum. Pseudo-resonances correspond to particular frequencies, where strong flow responses are triggered for specific spatial distributions of the forcing. These energy amplifications could be at the origin of the unsteadiness observed in noise amplifiers: low-level sustained upstream external perturbations can be amplified and filtered by the GLNS operator, leading to strong downstream unsteadiness characterized by broadband frequencies corresponding to the identified pseudo-resonances.

Optimal forcings are identified by achieving a singular value decomposition of the global resolvent operator. The outcome of this analysis is, for each frequency, optimal forcings, optimal responses, and optimal energy gains. The resolvent operator for the linearized Navier–Stokes operator has already been introduced in the local framework by Farrell et al. [15]. Here, we consider this operator in a global approach, in which the stream-wise direction is also solved. The singular value decomposition of the global resolvent matrix is a computationally challenging problem. The involved matrices stem from the spatial discretization of the GLNS operator, which results in large-scale matrices. The singular value decomposition has first been performed by considering reduced-order models based on global eigen-modes [16–18]. To obtain converged results, this approach requires a large number of global modes, which is a computationally challenging task. And it still suffers from convergence problems [19], especially for the optimal forcing structures. The direct computation of the dominant singular values on the large-scale problem without invoking global modes was first performed by Monokrousos et al. [20] using direct-adjoint simulations. This paper describes an alternative method based on a "discretize-then-optimize" scheme, which combines iterative Arnoldi methods and a direct LU solver. The proposed computational method is very efficient and enables to obtain not only the dominant singular value but also sub-optimals.

In a local approach, the study of noise amplifiers is usually achieved thanks to the e^N method, which evaluates the potential for energy extraction by integrating for a given frequency the local spatial amplification rate in the downstream direction. A precise comparison between the present approach and the e^N method can be achieved as they are both carried out in the frequency domain. This has not yet been done, since only global modes, that is, eigenvectors of the GLNS operator, have been compared to results obtained by the e^N method [21] and [16]. One of the objectives of this article is to make a thorough assessment of how the global singular modes relate to local results. In particular, there has been some debate during the past years concerning the spatial localization of the global singular modes with respect to local stability properties. For example, Akervik et al. [17] suggested in the case of Tollmien–Schlichting instabilities that the forcing structures might be localized near branch I. It could also be argued that the maximum of the optimal responses may be located near branch II. However, Akervik et al. [17] could not, however, assess these points since their computational domain did not comprise branch I and branch II at the analyzed frequency.

The present article also offers a physical discussion on the definition of amplification in globally stable open flows when studied using a frequency approach. In the case of oscillator flows, the temporal amplification rate of the unstable global modes gives the degree to which the flow is unstable. In the case of amplifier flows,

a quantification of the amplification mechanisms is provided by an input–output analysis. In the temporal domain, this quantification is usually defined as the ratio between the energy of the perturbations at a time $t = T$ (output) and at the initial time $t = 0$ (input). The value 1 of this energy gain defines without ambiguity the threshold between damping and amplification. The picture is less clear in the frequency domain where the quantification of the amplification mechanisms is usually defined as the ratio of the L_2 norm of the optimal response (output) with the L_2 norm of the optimal forcing (input). This definition is convenient from a mathematical perspective but lacks physical meaning as it compares two quantities with different physical dimensions, a kinetic energy integrated over space versus a squared acceleration integrated over space. As a consequence, the value 1 of this ratio does not clearly define the threshold between damping and amplification. We will address this issue by using an input–output approach based on the kinetic energy equations: the input is then the power supplied to the flow while the output refers to a kinetic energy flux. Finally, we will try to distinguish within the downstream spatial growth of the optimal response which part is due to the external optimal forcing or to an intrinsic amplification.

As an application of these concepts, the linear two-dynamics of a flat-plate boundary layer is considered. The three-dimensional dynamics is not studied in this paper. The physical results are therefore restricted to a boundary layer in low-level noise environment, for which the two-dimensional mechanisms are known to be predominant. This flow is well known to be a noise-amplifier flow, and two-dimensional perturbations may be amplified by two instability mechanisms. The long-term Tollmien–Schlichting instability takes advantage of the presence of a critical layer and a Stokes layer to impose a non-zero Reynolds stress. The short-term Orr instability [22] is observed for waves that lean against the mean shear. The amplification of such two-dimensional perturbation has been much studied within a local framework. Local stability analysis shows that the Blasius boundary layer is convectively unstable to Tollmien–Schlichting waves when the Reynolds number based on the local displacement thickness $\delta(x)$ is larger than the critical value 520. Eigenvalues of the local linearized Navier–Stokes operator then exhibit positive spatial growth rates. The flow configuration studied in this paper is chosen to obtain a local Reynolds numbers varying from 0 to 1,332. Within this choice, the location of branch I (respectively II), which spatially delimits the locally stable/unstable (respectively stable/unstable) regions, lay within the computational domain in the frequency range $30 \leq F \leq 240$ (respectively $80 \leq F \leq 240$). The results of the global approach and especially the structure of the singular modes optimal forcings/responses will be discussed in the light of these two instability mechanisms.

This article has some links with the works by Lopez et al. [23] and Do et al. [24]. These authors consider a Bödewadt boundary-layer flow on the stationary bottom end wall of a finite rotating cylinder. They look at the response of the flow to harmonic modulations of the rotation rate. They also call theses structures "Optimal harmonic responses" although the optimization parameter in their case is solely the frequency of modulation, since the forcing structure is fixed and given by the way they force the flow (modulations of the rotation rate of the cylinder). In the present study, the term "optimal" refers to an optimization over all frequencies and over the spatial distribution of the forcing structure.

The article proceeds as follows. First (Sect. 2), we introduce the singular value decomposition and present the new method, based on iterative Arnoldi methods and a direct LU solver, to compute the dominant singular vectors. Results concerning a flat-plate boundary layer where the leading edge is solved for are presented in Sect. 3. Dominant and sub-optimal structures will be analyzed and discussed in the light of the Orr and Tollmien–Schlichting instability mechanisms. A discussion (Sect. 4) follows, which addresses two issues raised above: a comparison of the global results with those given by a local theory (the e^N method) and a quantification of the amplifying behavior in terms of an energetic approach. Results will finally be summarized in Sect. 5.

2 Formalism

To investigate the dynamics of incompressible flows acting as noise amplifiers, we consider an input–output approach, consisting of the forced Navier–Stokes equations

$$\partial_t \boldsymbol{u} + \boldsymbol{u} \cdot \nabla \boldsymbol{u} = -\nabla p + \nu \nabla^2 \boldsymbol{u} + \epsilon \boldsymbol{f}', \quad \nabla \cdot \boldsymbol{u} = 0 \tag{1}$$

where the source term $\boldsymbol{f}'$ in the momentum equations models an external forcing and the parameter ϵ is introduced to tune its amplitude. The velocity and pressure fields $(\boldsymbol{u}, p)$ are decomposed into a steady component $(\boldsymbol{U}, P)$, the base-flow, and an unsteady component $\epsilon(\boldsymbol{u}', p')$, the perturbation. By introducing this decomposition into (1) and assuming a small amplitude forcing $\epsilon \ll 1$, we obtain at leading order that the base-flow is governed by the steady Navier–Stokes equations:

$$\boldsymbol{U}\cdot\boldsymbol{\nabla}\boldsymbol{U} = -\boldsymbol{\nabla}P + \nu\boldsymbol{\nabla}^2\boldsymbol{U}, \quad \boldsymbol{\nabla}\cdot\boldsymbol{U} = 0 \tag{2}$$

At next order, we obtain the equation governing the dynamics of linear perturbations developing onto the base-flow and triggered by the external forcing:

$$\partial_t\boldsymbol{u}' + \boldsymbol{U}\cdot\boldsymbol{\nabla}\boldsymbol{u}' + \boldsymbol{u}'\cdot\boldsymbol{\nabla}\boldsymbol{U} = -\boldsymbol{\nabla}p' + \nu\boldsymbol{\nabla}^2\boldsymbol{u}' + \boldsymbol{f}', \quad \boldsymbol{\nabla}\cdot\boldsymbol{u}' = 0 \tag{3}$$

In the case of noise amplifiers, the base-flow is globally stable. Thus, at large times and without forcing ($\epsilon = 0$), any initial perturbation superimposed onto the base-flow will vanish even if it can be largely amplified in short times. Here, we are interested rather by the long-time dynamics when the flow is continuously subject to external forcing. The role of the external forcing is thus to sustain the perturbation, and we wish to determine the characteristics of the external forcing (for instance, its frequency and spatial location), which lead to the largest amplitude perturbations.

It is therefore natural to consider a Fourier decomposition of the forcing and response. These quantities may thus be considered as harmonic waves of real frequency ω:

$$\mathbf{f}'(x,y,t) = \hat{\mathbf{f}}(x,y)\mathrm{e}^{\mathrm{i}\omega t} + \text{c.c.} \tag{4}$$

$$(\mathbf{u}',p')(x,y,t) = (\hat{\mathbf{u}},\hat{p})(x,y)\mathrm{e}^{\mathrm{i}\omega t} + \text{c.c.} \tag{5}$$

where $\hat{\mathbf{f}}$ and $(\hat{\mathbf{u}},\hat{p})$ indicate the (complex) structures of the forcing and response waves respectively. Introducing this decomposition into (3), we obtain the equations

$$\mathrm{i}\omega\hat{\boldsymbol{u}} + \boldsymbol{U}\cdot\boldsymbol{\nabla}\hat{\boldsymbol{u}} + \hat{\boldsymbol{u}}\cdot\boldsymbol{\nabla}\boldsymbol{U} = -\boldsymbol{\nabla}\hat{p} + \nu\boldsymbol{\nabla}^2\hat{\boldsymbol{u}} + \hat{\boldsymbol{f}}, \quad \boldsymbol{\nabla}\cdot\hat{\boldsymbol{u}} = 0 \tag{6}$$

that govern the spatial structure of the perturbation $\hat{\boldsymbol{u}}$ driven by a wave of spatial structure $\hat{\boldsymbol{f}}$ and frequency ω. For convenience, we rewrite these equations in a compact form

$$\hat{\mathbf{u}} = \mathcal{C}(\omega)\hat{\mathbf{f}} \tag{7}$$

where $\mathcal{C} = \mathcal{P}^T\,(\mathrm{i}\omega\mathcal{B} - \mathcal{A})^{-1}\,\mathcal{P}$ is known as the resolvent operator. Here, $\mathcal{B} = \mathcal{P}\mathcal{P}^T$ and $\mathcal{P}$ is the prolongation operator that transforms a velocity vector $(u,v)^T$ into a velocity–pressure quantity $(u,v,0)^T$, and its transpose is the restriction operator. $\mathcal{A}$ denotes the linearized Navier–Stokes operator around the base-flow

$$\mathcal{A} = \begin{pmatrix} -\mathbf{U}\cdot\boldsymbol{\nabla} - ()\cdot\boldsymbol{\nabla}\mathbf{U} + \nu\boldsymbol{\nabla}^2 & -\boldsymbol{\nabla} \\ \boldsymbol{\nabla}\cdot() & 0 \end{pmatrix}. \tag{8}$$

We now look for forcings $\hat{\mathbf{f}}$, which yield the strongest responses $\hat{\mathbf{u}}$. This corresponds to an optimization problem for the forcing $\hat{\mathbf{f}}$. Usually, there are two approaches [25] to solve an optimization problem. The continuous approach consists to first define a continuous optimization problem and then discretize it whereas the discrete approach consists to discretize the governing equations before defining an optimization problem. In the following, we will choose the second option. The main reason is that the discretize-then-optimize strategy is superior to the optimize-then-discretize strategy in terms of accuracy and well-posedness of the numerical problems. But one has to keep in mind that, even though we present the forthcoming developments in a discrete approach, the structures that we will introduce do have an intrinsic (continuous) existence that does not depend on the nature of the chosen discretization.

Once a spatial discretization has been chosen, the governing Eq. (7) reads:

$$\hat{\mathbf{u}} = \mathbf{C}(\omega)\hat{\mathbf{f}} \tag{9}$$

where $\mathbf{C}(\omega) = \mathbf{P}^T\,(\mathrm{i}\omega\mathbf{B} - \mathbf{A})^{-1}\,\mathbf{P}\mathbf{M}$. Here, $\mathbf{B}$, $\mathbf{A}$, $\mathbf{M}$, and $\mathbf{P}$ are large-scale matrices, which are sparse in the case of finite difference or finite element discretizations. The definition of the discrete resolvent is similar to the continuous resolvent (see Eq. 7), except for the introduction of the matrix $\mathbf{M}$ that depends on the chosen spatial discretization. For instance, it is defined as the identity matrix $\mathbf{M} = \mathbf{I}$ in the case of finite differences while in a finite element approach, $\mathbf{M}$ designates the mass-matrix. $\mathbf{P}$ is the prolongation matrix, which takes a velocity vector and adds zero pressure components to yield a velocity–pressure vector, while $\mathbf{P}^T$ is the restriction operator, which extracts the velocity components from a velocity–pressure vector. Note that the superscript ^{T} designates the transpose, while * is the trans-conjugate. Finally, the matrix $\mathbf{B}$ is defined by $\mathbf{B} = \mathbf{P}\mathbf{M}\mathbf{P}^T$ so that $\mathrm{i}\omega\mathbf{B} - \mathbf{A}$ is the global linearized Navier–Stokes matrix in the frequency domain.

To measure the degree of amplification of the perturbations, we consider global measures of the response and forcing. We look for optimal forcings $\hat{\mathbf{f}}$, which maximize the gain:

$$G(\hat{\mathbf{f}}) = \frac{\hat{\mathbf{u}}^* \mathbf{Q}_u \hat{\mathbf{u}}}{\hat{\mathbf{f}}^* \mathbf{Q}_f \hat{\mathbf{f}}} \tag{10}$$

where $\hat{\mathbf{u}} = \mathbf{C}(\omega)\hat{\mathbf{f}}$. Here, $\mathbf{Q}_u$ and $\mathbf{Q}_f$ are two hermitian matrices defining the global measures of the response and forcing. $\mathbf{Q}_f$ is meant to be positive definite whereas $\mathbf{Q}_u$ is positive but may have a non-zero null-space [26]. For example, $\hat{\mathbf{u}}^* \mathbf{Q}_u \hat{\mathbf{u}}$ may stand for the energy in some sub-domain Ω_u while $\hat{\mathbf{f}}^* \mathbf{Q}_f \hat{\mathbf{f}}$ is the energy in the whole computational domain Ω. Note that G corresponds to the ratio of two quantities of different physical dimensions: the numerator refers to the kinetic energy of the perturbation while the denominator is the energy of the forcing. The quantitative value of G has therefore no physical meaning: G has been chosen because the related optimization problem is mathematically well-posed. A more physical quantity referring to the true amplification will be introduced in Sect. 4.2 based on an energetic input–output approach.

This optimization problem is readily solved by studying the generalized (with respect to the matrices $\mathbf{Q}_f$ and $\mathbf{Q}_u$) singular value decomposition of the global resolvent:

$$\mathbf{C}(\omega) = \hat{\mathbf{U}} \Lambda \hat{\mathbf{F}}^* \mathbf{Q}_f \tag{11}$$

$$\hat{\mathbf{U}}^* \mathbf{Q}_u \hat{\mathbf{U}} = \hat{\mathbf{F}}^* \mathbf{Q}_f \hat{\mathbf{F}} = \mathbf{I} \tag{12}$$

where the matrix Λ is a diagonal matrix with positive entries λ_i, called the singular values. The singular values are ranked by decreasing value $\lambda_1 \geq \lambda_2 \geq \cdots$. The columns of the two matrices $\hat{\mathbf{U}}$ and $\hat{\mathbf{F}}$ are respectively called the left and right (generalized) singular vectors and will be denoted $\hat{\mathbf{u}}_i$ and $\hat{\mathbf{f}}_i$. The orthonormality relations (12) express that these singular vectors are orthonormal with respect to the inner products associated with $\mathbf{Q}_u$ and $\mathbf{Q}_f$, that is, $\hat{\mathbf{u}}_i^* \mathbf{Q}_u \hat{\mathbf{u}}_j = \delta_{ij}$ and $\hat{\mathbf{f}}_i^* \mathbf{Q}_f \hat{\mathbf{f}}_j = \delta_{ij}$ where δ_{ij} stands for the Kronecker symbol. One may verify from Eqs. (11) and (12) that the left and right singular vectors are linked through:

$$\mathbf{C}(\omega)\, \hat{\mathbf{f}}_i = \lambda_i \hat{\mathbf{u}}_i \tag{13}$$

This equation yields a physical interpretation of the singular values and vectors. A right singular vector $\hat{\mathbf{f}}_i$ corresponds to an external forcing structure of unit energy $\hat{\mathbf{f}}_i^* \mathbf{Q}_f \hat{\mathbf{f}}_i = 1$. The response of the flow to this forcing is given by $\lambda_i \hat{\mathbf{u}}_i$, where the left singular vector $\hat{\mathbf{u}}_i$ represents the spatial structure (of unit energy $\hat{\mathbf{u}}_i^* \mathbf{Q}_u \hat{\mathbf{u}}_i = 1$) of the flow response and the singular value λ_i designates its global amplitude. In the following, the left and right singular vectors will be called the optimal responses and optimal forcings, respectively.

Now, let us show how this decomposition straightforwardly characterizes the global frequency response for any given forcing $\hat{\mathbf{f}}$. The expansion of this forcing onto the set of optimal forcings is given as $\hat{\mathbf{f}} = \sum_{i=1}^{N} \alpha_i \hat{\mathbf{f}}_i$ where the complex coefficients α_i are readily obtained as the scalar products of the forcing $\hat{\mathbf{f}}$ with the corresponding optimal forcings, that is, $\alpha_i = \hat{\mathbf{f}}_i^* \mathbf{Q}_f \hat{\mathbf{f}}$. The energy of the forcing is then given by $\hat{\mathbf{f}}^* \mathbf{Q}_f \hat{\mathbf{f}} = \sum_{i=1}^{N} |\alpha_i|^2$ which shows that the magnitude of the coefficient $|\alpha_i|$ is related to the fraction of forcing energy accounted for by the ith optimal forcing. If we introduce this forcing expansion into the frequency response problem (9), we obtain the flow response as an expansion in terms of optimal responses

$$\hat{\mathbf{u}} = \sum_{i \geq 1} \lambda_i \alpha_i \hat{\mathbf{u}}_i \tag{14}$$

This relation is central to the whole approach, since for a given forcing $\hat{\mathbf{f}}$, it straightforwardly yields the response of the flow $\hat{\mathbf{u}}$. The expansion coefficients $\lambda_i \alpha_i$ are related to the fraction of energy accounted for by the ith optimal response. Since the optimal response basis $\hat{u}_i$ is orthonormal, the energy of the response $\hat{\mathbf{u}}$ is simply given by:

$$\hat{\mathbf{u}}^* \mathbf{Q}_u \hat{\mathbf{u}} = \sum_{i \geq 1} \lambda_i^2 |\alpha_i|^2 \tag{15}$$

For example, if $\lambda_1 \gg \lambda_2$, in order to have a maximum response of the flow, one should excite at the frequency ω where the curve $\lambda_1(\omega)$ is maximum and with a structure that is closest to $\hat{\mathbf{f}} = \hat{\mathbf{f}}_1(\omega)$. The resulting flow

would then have the same structure as $\hat{\mathbf{u}}_1$ with an energy equal to $\hat{\mathbf{u}}^* \mathbf{Q}_u \hat{\mathbf{u}} = \lambda_1^2$. The dominant optimal forcing $\hat{\mathbf{f}}_1$ therefore identifies a receptive region of the flow, that is, a region where a small amplitude forcing triggers a large flow response.

The numerical computation of the singular values of the global resolvent is based on the reformulation of the singular value problem as an eigenvalue problem. The singular values λ_i and right singular vectors $\hat{\mathbf{f}}_i$ can be found by solving the generalized eigenvalue problem

$$\mathbf{D}\,\hat{\mathbf{f}}_i = \lambda_i^2 \mathbf{Q}_f \hat{\mathbf{f}}_i \tag{16}$$

where the matrix $\mathbf{D} = \mathbf{C}(\omega)^*\,\mathbf{Q}_u\,\mathbf{C}(\omega)$ is hermitian. We may hence normalize the eigenvectors as $\hat{\mathbf{f}}_i^* \mathbf{Q}_f \hat{\mathbf{f}}_i = 1$, and the left singular vectors $\hat{\mathbf{u}}_i$ can be found by solving (13). The generalized eigenvalue problem (16) is finally recast in a standard eigenvalue problem by considering the matrix $\mathbf{Q}_f^{-1}\mathbf{D}$. Its largest eigenvalues are computed using the ARPACK's library [27] in regular mode and complex arithmetic (driver znaupd, http://www.caam.rice.edu/software/ARPACK/). Hence, it is required at each step to compute $\mathbf{Q}_f^{-1}\mathbf{D}\mathbf{w}$ for a given complex vector $\mathbf{w}$. For this, we note that $\mathbf{Q}_f^{-1}\mathbf{D} = \mathbf{Q}_f^{-1}\mathbf{M}^T\mathbf{P}^T(\mathbf{L}^*)^{-1}\mathbf{P}\mathbf{Q}_u\mathbf{P}^T\mathbf{L}^{-1}\mathbf{P}\mathbf{M}$ with $\mathbf{L} = \mathrm{i}\omega\mathbf{B} - \mathbf{A}$. Hence, for a given $\mathbf{w}$, we apply in sequence all the operators appearing in this expression. The inverse $\mathbf{Q}_f^{-1}$ may be handled by a conjugate gradient, so that the bottleneck of this algorithm is the computation of $\mathbf{L}^{-1}\mathbf{w}$ and $(\mathbf{L}^*)^{-1}\mathbf{w}$. In the present work, we explicitly form the sparse matrix $\mathbf{L}$ and invert it using a sparse direct LU solver (MUMPS package[28], http://graal.ens-lyon.fr/MUMPS/). In terms of storage, only the matrix $\mathbf{L}$ has to be once LU decomposed since this matrix is involved in both inverses. Hence, the overall cost of the algorithm is the cost of one LU decomposition.

3 Results

The formalism developed in the previous section has been applied to a flat-plate two-dimensional boundary-layer flow. The flow configuration and the base-flow are described in the first subsection. Results of the singular value analysis are presented in the second subsection.

3.1 Flow configuration and base-flow

We consider a two-dimensional boundary layer developing over a flat plate of length 1.25. A uniform free-stream velocity ($u = u_\infty = 1, v = 0$) imposed at the inlet boundary ($x = -0.5, 0 \le y \le 1$) develops and encounters a flat plate located on the segment ($0 \le x \le 1.25, y = 0$) where no-slip boundary conditions are enforced. Symmetric boundary conditions are applied on the boundaries ($-0.5 \le x < 0, y = 0$) and ($-0.5 \le x \le 1.25, y = 1$). Standard outflow boundary conditions are used at the outlet boundary ($x = 1.25, 0 \le y \le 1$): $-\hat{p}\mathbf{n} + \nu\nabla\hat{\mathbf{u}} \cdot \mathbf{n} = 0$. The Reynolds number based on the length $l = 1$ and on the free-stream velocity $u_\infty = 1$ is fixed to $Re = 6 \times 10^5$. In the following, the stability of the boundary layer is investigated in the restricted domain $Re_x = u_\infty x/\nu \le Re$, which implies that the optimization domain is defined as $x \le l$, where $l = 1$. This means that we look for forcings $\hat{\mathbf{f}} = (f, g)$, which optimize the ratio between the perturbation energy $\hat{\mathbf{u}}^*\mathbf{Q}_u\hat{\mathbf{u}} = \int\int_{x\le l}(|u|^2 + |v|^2)\mathrm{d}x\mathrm{d}y$ and the forcing energy $\hat{\mathbf{f}}^*\mathbf{Q}_f\hat{\mathbf{f}} = \int\int(|f|^2 + |g|^2)\mathrm{d}x\mathrm{d}y$. Note that changing the length of the optimization domain l is equivalent to changing the Reynolds number $Re = u_\infty l/\nu$. The computational domain extends up to $x = 1.25$ to insure that the downstream boundary condition does not affect the results within the optimization domain. This has been checked in detail in "Appendix".

The base-flow is governed by the steady Navier–Stokes equation: with the above-mentioned boundary conditions holding for the velocity field $\boldsymbol{U} = (U, V)$. A Newton method is used to solve this non-linear equation, and the spatial derivatives are discretized with Taylor-Hood finite elements ($P2$ elements for the velocity field and $P1$ elements for the pressure). The mesh consists of 3.03×10^6 triangles, and their size in the boundary-layer region ($-0.5 \le x \le 1.25, 0 \le y \le 0.02$) is $\Delta x = 1/6{,}000$. This results in a number of degrees of freedom equal to 13.7×10^6. The displacement thickness of the numerical solution is in agreement with the analytic expression $1.72Re^{-1/2}\sqrt{x}$ obtained for the asymptotic Blasius similarity solution (see Fig. 1). The Reynolds number based on the local displacement thickness $Re_{\delta(x)}$ increases from 0 at the sharp leading edge

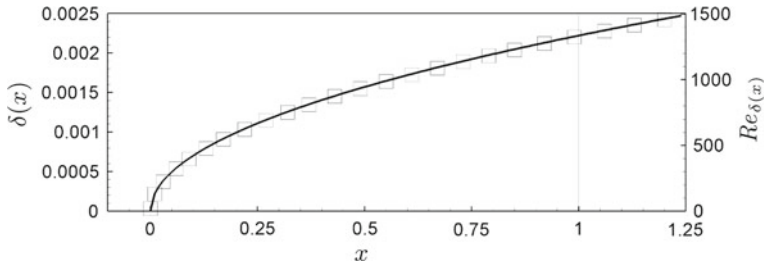

Fig. 1 $Re = 6 \times 10^5$. Displacement thickness $\delta(x)$ and associated local Reynolds number $Re_{\delta(x)}$ of the two-dimensional base-flow (*symbols*) and of the analytic self-similar Blasius solution (*line*). The *vertical solid line* shows the downstream limit of the domain of interest $Re_x \leq Re$.

to 1,332 at $x = 1$ and reaches 1,490 at the outlet ($x = 1.25$). In the following, $\delta = 1.72/\sqrt{Re}$ will designate the displacement thickness at the coordinate $x = 1$. Also, as done in previous studies on boundary layers, we will use the frequency $F = 10^6 \cdot \omega/Re$ instead of ω to present the results.

3.2 Optimal forcings/responses

For $F = 100$, the largest energy gains are equal to $\lambda_1^2 = 198.7$, $\lambda_2^2 = 2.1$, and $\lambda_3^2 = 0.87$. The optimal forcing $\hat{\mathbf{f}}_1$ and response $\lambda_1 \hat{\mathbf{u}}_1$ associated with the first singular value are depicted in Fig. 2a, b by the iso-contours of the real part of their stream-wise component. In Fig. 2e, we have represented in black dashed line and black solid line, the energy density functions $d_f(x) = \int_0^1 (|f|^2 + |g|^2) \mathrm{d}y$ and $d_u(x) = \int_0^1 (|u|^2 + |v|^2) \mathrm{d}y$. The dominant optimal response $\lambda_1 \hat{\mathbf{u}}_1$ is localized downstream around $x = 0.90$, very close to branch II located at $x = 0.86$. The mode exhibits a 180 degrees phase reversal in the wall-normal direction, characteristic of the Tollmien–Schlichting instability. The imaginary part of the optimal response (not depicted here) is similar to the real part but out of phase, thus enabling a continuous downstream convection of the perturbations. The optimal forcing $\hat{\mathbf{f}}_1$ is localized upstream near $x = 0.30$, where branch I is located. It consists of elongated waves inclined against the flow stream. This spatial structure indicates that the Orr mechanism is at play to extract energy from the base-flow. These forcing/response structures are similar to those shown by Monokrousos et al. [20], except that theirs were pinned at the upstream and downstream boundaries of the computational domain. Indeed, their flow configuration does not include branch I and branch II within their computational domain. The forcing and response associated with the second singular value, shown in Fig. 2c, d, are similar to those related to the dominant singular value, except that they present two maxima in the stream-wise direction. These results are reminiscent of the fact that the forcing and response bases are orthogonal. Unlike the dominant singular modes, there is no clear stream-wise separation (upstream and downstream) between the forcing $\hat{\mathbf{f}}_2$ and the response $\lambda_2 \hat{\mathbf{u}}_2$. The structure of the forcing indicates that a residual Orr mechanism contributes to the energy gain λ_2^2.

Figure 3a shows the largest energy gains λ_1^2, λ_2^2 and λ_3^2 as a function of the frequency F. For λ_1^2, the maximum response is obtained for the frequency $F = 88$ indicating that a preferred frequency exists for the extraction of energy within the domain $x \leq 1$. It is nearly three orders of magnitude higher than the second and third singular values. This large gain corresponds to a pseudo-resonance since it cannot be simply explained by the presence of a particular eigenvalue in the spectrum of the linearized Navier–Stokes operator around the real frequency $F = 88$ [16,17]. To investigate the stream-wise distribution of the dominant optimal forcing $\hat{\mathbf{f}}_1$ and response $\lambda_1 \hat{\mathbf{u}}_1$ as a function of frequency, the energy density functions $d_u(x)$ and $d_f(x)$ are shown in the $(Re_{\delta(x)}, F)$ plane in Fig. 3b, c. The spatial support of the optimal forcing and response are located upstream and downstream, respectively. This spatial separation of the forcing and response is analogous to the separation of the adjoint and direct global eigen-modes, which has been viewed as a footprint of the convective non-normality in open flows [6,7]. The loci of the maxima of the energy density functions within the domain $x \leq 1$ are shown by the cyan symbols. For comparison, the neutral curve obtained from a local linear stability analysis of the profiles extracted at each stream-wise position is shown with the magenta line. The optimal forcings exhibit a peak at the convectively stable/unstable boundary (branch I) whereas the optimal responses are maximum at the convectively unstable/stable boundary (branch II). The agreement is particularly good for the position of the optimal forcing and only deteriorates for high frequency ($F \geq 210$) and low frequency ($F \leq 50$).

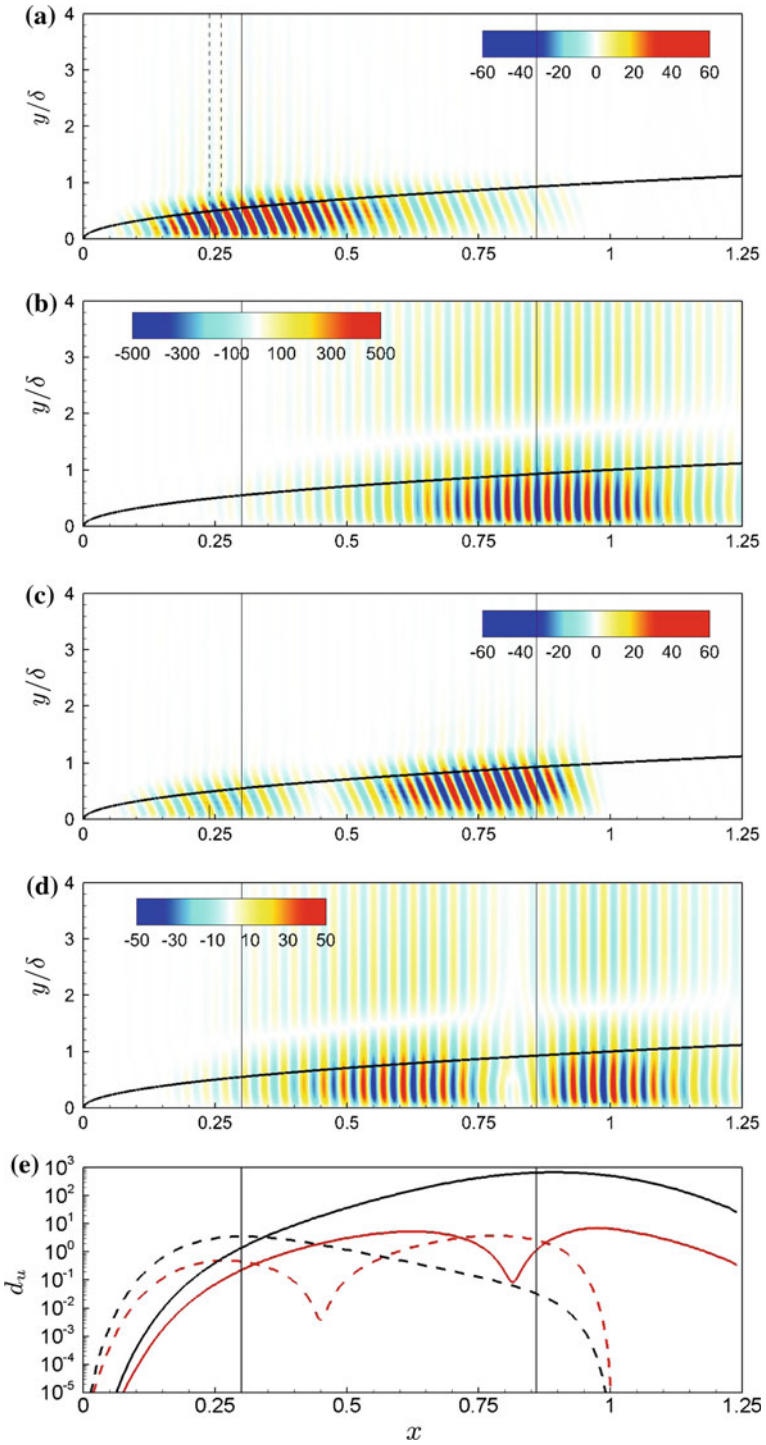

Fig. 2 Results for $Re = 6 \times 10^5$ and $F = 100$. **a** Real part of stream-wise momentum forcing $\hat{\mathbf{f}}_1$ for dominant singular value. **b** Real part of stream-wise velocity response $\lambda_1 \hat{\mathbf{u}}_1$. **c**, **d** Same for second singular value. **e** Energy density functions $d_f(x)$ (*dashed lines*) and $d_u(x)$ (*solid lines*) for first (*black lines*) and second (*red lines*) singular modes. The *vertical dashed lines* in **a** refer to the location of the stream-wise localized forcing introduced in Sect. 4.1 while the *vertical solid lines* show branch I and branch II in **a**–**e**. The *thick solid line* in **a**–**d** indicate the local displacement thickness $\delta(x)$ (color figure online)

The maximum of the optimal response is slightly shifted downstream from branch II for increasing frequency. These slight disagreements may be explained either by non-parallel effects [29] or by the Orr mechanism, both not accounted for in the local modal stability analysis. In a global setting, the Orr and Tollmien–Schlichting

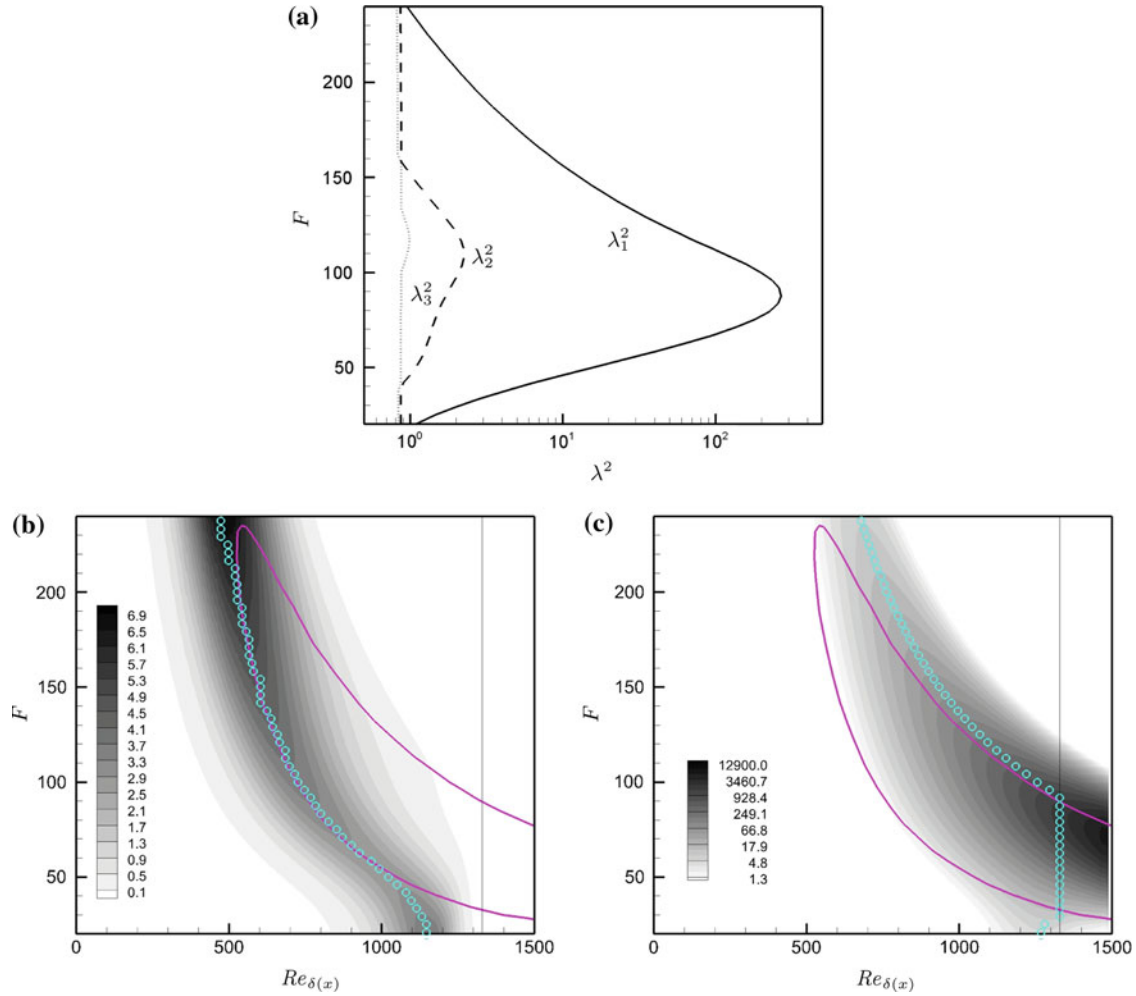

Fig. 3 $Re = 6 \times 10^5$. **a** Optimal gains as a function of the frequency F. **b** Iso-values of energy density for the dominant optimal forcing $\hat{\mathbf{f}}_1$ in the $(Re_{\delta(x)}, F)$ plane. **c** Same for optimal response $\lambda_1 \hat{\mathbf{u}}_1$. The *curve* defined by *cyan symbols* yields for a given frequency F the maximum of the energy density function within $x \leq 1$. The *magenta curve* designates the neutral curve as obtained from a local stability analysis. The *vertical black solid lines* show the optimization region $x \leq 1$ ($Re_{\delta(x)} \leq 1{,}332$) (color figure online)

mechanisms are in competition and both contribute to the energy gain. At high frequency $F \geq 210$, the locally unstable region decreases in size due to a weakening of the Tollmien–Schlichting mechanism. Thus, the Orr mechanism becomes dominant. At low frequency $F \leq 50$, the locally unstable region is outside the optimization domain $x \leq 1$ and the Orr mechanism is again dominant.

Inspection of Fig. 3b, c yields some interesting information about the dependance of the dominant singular value λ_1^2 with respect to the Reynolds number Re or equivalently to the distance l defining the optimization region. For high frequencies ($F > 130$), both the optimal forcing and the optimal response are located far inside the optimization domain, with small values of the density functions near $x = l = 1$. The optimal gains in this frequency range therefore do not depend on the Reynolds number Re, provided $Re \geq 6 \times 10^5$. For intermediate frequencies ($50 < F < 130$), only the optimal forcing is located far inside the optimization region while the optimal response displays strong energy density values at the end of the optimization domain near $x = l = 1$. The optimal gain λ_1^2 being the ratio between the energy of the optimal response and the energy of the optimal forcing is therefore an explicit function of the Reynolds number Re. For example, if this Reynolds number is slightly increased above 6×10^5, the energy of the optimal response will increase while keeping the energy of the optimal forcing constant: as a result, the singular value λ_1^2 increases, that is, $\mathrm{d}\lambda_1^2/\mathrm{d}Re > 0$. For this intermediate range of frequencies, we therefore obtain lower bounds for the optimal gains (with respect to their asymptotic values reached at higher Reynolds numbers). For low frequencies $F < 50$, both the optimal

forcing and the optimal response display strong energy densities close to $x = l = 1$ and the optimal gain strongly depends on the optimization domain. In this last case, there is no guarantee that $\mathrm{d}\lambda_1^2/\mathrm{d}Re \geq 0$ near $Re = 6 \times 10^5$. Note that for a given Reynolds number Re defining the optimization domain, there always exists a frequency threshold below (respectively above), which the optimal gain is dependant (respectively independent) of the Reynolds number. This is due to the fact that branch I and branch II move downstream (toward increasingly high Reynolds numbers $Re_{\delta(x)}$) as the frequency F tends to zero in the case of the TS instability.

4 Discussion

This section is dedicated to two specific points. The first paragraph investigates how the optimal forcing and response structures may be used to approximate the flow response to a localized forcing. The results are compared with the e^N method, which has widely been used to characterize amplifier flows in weakly-non-parallel flows. The second paragraph introduces a quantification of the amplification based on an input–output energetic approach.

4.1 The signaling problem: approximation with singular modes and with local approach

Let us first consider a flow forced by the optimal forcing $\hat{\mathbf{f}} = \hat{\mathbf{f}}_1$ at frequency $F = 100$. The associated exact response is given by the optimal response $\hat{\mathbf{u}} = \lambda_1 \hat{\mathbf{u}}_1$. The energy densities d_f and d_u have already been discussed in Fig. 2e. The energy growth of the response $d_u^{-1}(\mathrm{d}/\mathrm{d}x)(d_u)$ is shown as a function of x with dashed lines in Fig. 4b. The spatial amplification rate obtained from a local stability theory is given in thin solid line. We observe that the latter poorly reproduces the exact energy growth in the region where the forcing is strong ($0.25 \leq x \leq 0.4$). This is not surprising since the local results are known to be valid only downstream of any forcing.

To address a suitable comparison with the local approach, we consider a forcing $\hat{\mathbf{f}}(x, y)$ at frequency $F = 100$ that is localized upstream of branch I ($x = 0.30$). Its spatial structure is chosen as the optimal forcing $\hat{\mathbf{f}}_1$ in the range $x \in [0.25 - 5\delta, 0.25 + 5\delta]$ and zero elsewhere. For clarity, this region is delimited by the

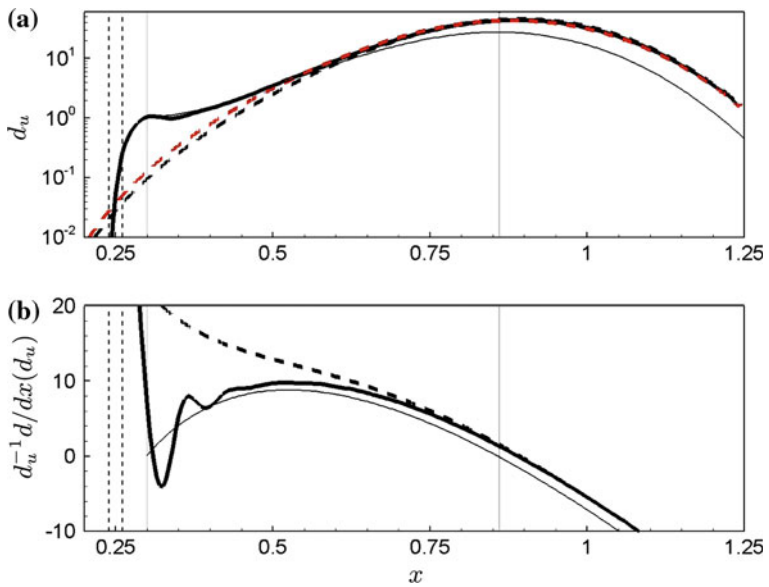

Fig. 4 $Re = 6 \times 10^5$. Forcing localized at $x = 0.25$ with frequency $F = 100$. **a** Energy density of response. **b** Spatial energy growth of response. *Thick solid line* exact global solution, *thin solid line* local solution, *black* and *red dashed lines* approximation with 1 and 2 singular modes. The *vertical dashed lines* refer to the location of the stream-wise localized forcing while the *vertical solid lines* show branch I and branch II. Note that the *dashed-* and *thin solid lines* in **b** may also be considered to analyze the case of the response to the forcing $\hat{\mathbf{f}} = \hat{\mathbf{f}}_1$ (see first paragraph of Sect. 4.1) (color figure online)

Table 1 Approximated response to stream-wise localized forcing using the singular modes

i or N	$\lvert\alpha_i\rvert^2$	$E^N_{\hat{\mathbf{f}}}$	λ_i^2	$\lambda_i^2\lvert\alpha_i\rvert^2$	$E^N_{\hat{\mathbf{u}}}$
1	0.0679	0.0679	198.66	13.485	13.485
2	0.0105	0.0784	2.096	0.022	13.507
3	0.0023	0.0807	0.873	0.002	13.509
4	0.0164	0.0971	0.869	0.014	13.523
5	0.0048	0.1019	0.827	0.00002	13.523
∞	–	1	–	–	13.553

The first column gives the truncation parameter N or the numbering of singular mode i. The second and third columns give the forcing energy captured by the ith optimal forcing and by the first N forcing modes, respectively. The fourth column is the optimal gain associated with the ith singular mode. The fifth and sixth columns give respectively the energy contained in the ith optimal response and in the first N response modes. The last line stands for the exact solution referred by $N = \infty$ for convenience

vertical dashed lines in Fig. 2. After rescaling the forcing to unit energy, that is, $\hat{\mathbf{f}}^*\mathbf{Q}_f\hat{\mathbf{f}} = 1$, the exact response is straightforwardly obtained with the direct solver by computing $\hat{\mathbf{u}} = \mathbf{C}\hat{\mathbf{f}}$.

Approximations of the imposed forcing and corresponding flow response can be obtained from the singular modes as

$$\hat{\mathbf{f}} \sim \sum_{i=1}^{N} \alpha_i \hat{\mathbf{f}}_i \ , \quad \hat{\mathbf{u}} \sim \sum_{i=1}^{N} \alpha_i \lambda_i \hat{\mathbf{u}}_i \ , \quad \alpha_i = \hat{\mathbf{f}}_i^* \mathbf{Q}_f \hat{\mathbf{f}} \tag{17}$$

where N is a truncation parameter. The coefficient α_i is defined as the projection of the imposed forcing onto the optimal forcing and determines the contribution of $\hat{\mathbf{f}}_i$ to $\hat{\mathbf{f}}$. The contribution of each optimal response structure to the exact solution is given by the product $\alpha_i\lambda_i$ of this coefficient with the singular value. The energy of the approximated forcing and response is then obtained as

$$E^N_{\hat{\mathbf{f}}} = \sum_{i=1}^{N} |\alpha_i|^2 \ , \quad E^N_{\hat{\mathbf{u}}} = \sum_{i=1}^{N} \lambda_i^2 |\alpha_i|^2 \tag{18}$$

since the optimal forcings and optimal responses form two orthonormal bases. Results obtained using up to five singular modes are presented in Table 1. As shown in the last column, the energy captured by the first optimal response (13.485) corresponds to more than 99 % of the energy of the exact response (13.553). The other optimal responses contribute very weakly to the energy response. It is interesting to note that their contribution is not necessarily ordered. For instance, the energetic contribution of the fourth optimal response is larger than the third one. This is not due to the ranking of the singular values λ_i^2, which is decreasing by construction. It rather stems from the contributions $|\alpha_i|^2$ to the forcing, which are not ordered as seen in the second column. Surprisingly their values are very weak. The first optimal forcing mode captures 6.79 % of the exact forcing energy, and the five optimal forcing modes only capture 10 %. It shows that only a small fraction of the forcing energy is used to trigger almost all of the energy of the response.

To further address the comparison, we examine how the energy of the flow response is locally approximated by singular modes. The local energy density $d_u(x)$ of the response is plotted as a function of the stream-wise location in Fig. 4a. The thick solid line is the exact solution while the black and red dashed lines are the approximated solutions with $N = 1$ and $N = 2$, respectively. The exact solution displays a strong amplification within the forcing region, exemplified in the figures by the vertical dashed lines, as well as immediately downstream. The growth outside of the forcing region is attributed to the Orr mechanism since the stream-wise localized forcing exhibits a spatial pattern of upstream-tilted vortices. Further downstream, the energy amplification is due to the Tollmien–Schlichting instability. Using only the first singular mode, the local energy of the approximated solution is close to the exact one for $x > 0.5$. A slight overestimation is observed around the maximum of the flow response, but this mismatch nearly disappears when using two singular modes. Just downstream of the forcing region, the truncated solution underestimates the local energy of the exact response even when using two singular modes. This difference could probably be minimized using more singular modes. However, it would barely modify the total energy of the response, as noticed previously (see Table 1), because the local energy in this region is two orders of magnitude smaller than at its maximal value. Turning now to the local approach, the energy density of the flow response is estimated via the so-called e^N method. It consists in integrating in the stream-wise direction the amplification rate of

one spatial mode at a given frequency. A reference amplitude needs to be defined. At a starting position, here the location of branch I ($x = 0.30$ for this frequency), the energy of the local approximation is chosen equal to the local energy of the exact solution. This local approximation is depicted by the thin solid line in Fig. 4a. It underestimates the exact energy by a factor of two at the maximum $x = 0.90$.

A last comparison is performed by examining the local energy growth, that is, the stream-wise derivatives of the curves shown in Fig. 4a. The results are displayed in Fig. 4b with the same convention as in Fig. 4a. The energy growth of the exact response is irregular close to the forcing location ($0.25 \leq x \leq 0.45$) and displays a monotonous variation further downstream $x \geq 0.45$. This monotonous variation is well reproduced by the local energy growth, but the exact energy growth is always underestimated. This constant error is cumulative in the e^N method and results in the factor 2 error mentioned above. Close to the forcing location, the comparison is quite poor. These observations may be understood by recalling that the local theory yields a good approximation of the energy growth if the flow is parallel and if the comparison is done far downstream from the excitation so that only the first local spatial mode dominates the solution. Close to the forcing location, many local spatial modes are excited by the forcing, which explains the poor comparison. Further downstream (for $x \geq 0.50$), the mismatch between the thick and thin curves stems from the non-parallelism of the flow. The approximation given by the first singular value yields good results only for $x \geq 0.75$. This stems from the fact that this solution was built to approximate the overall energy of the solution and not the spatial energy growth. Yet, as low energy levels are involved in the region $x \leq 0.75$, the mismatch in terms of spatial energy growth does not affect the performance for the energy density shown in Fig. 4a. To conclude, local and global approaches are inherently different: the local theory targets the spatial energy growth while the singular modes approximate the overall energy with dynamical structures. It should be added that the local results might be improved by considering a weakly-non-parallel approach such as the "Parabolized Stability Equations" method and more than one spatial mode.

4.2 Quantification of amplifying behavior

One of the objectives of the present article is to characterize the degree of amplification in a globally stable open flow. As mentioned in the introduction, a quantification of the instability is obtained by comparing input and output quantities. We have seen that the optimal energy gain is not a suitable quantity for this since it corresponds to a ratio involving two quantities of different physical dimensions. Another idea would be to evaluate the energy amplification of the dominant optimal response $\lambda_1 \mathbf{u}_1$ between two stream-wise stations x_0 (the input) and x_1 (the output). This strategy is followed by the e^N method in the local approach. It reduces to evaluating the ratio $d_u(x_1)/d_u(x_0)$, with $d_u(x)$ as the energy density function of $\lambda_1 \hat{\mathbf{u}}_1$. Yet this quantity is meaningful only if the optimal forcing $\hat{\mathbf{f}}_1$ is small between x_0 and x_1; otherwise, $\hat{\mathbf{f}}_1$ can be considered as a supplementary input that is not taken into account in the ratio $d_u(x_1)/d_u(x_0)$. From the analysis of the black dashed line in Fig. 2e, we can see that the amplitude of $\hat{\mathbf{f}}_1$ is small only if x_0 and x_1 are chosen far downstream, that is, at least $x_1 > x_0 > 0.5$. Now, between branch I ($x = 0.3$) and $x = 0.5$, both the energy growth of the optimal response $\lambda_1 \hat{\mathbf{u}}_1$ and the amplitude of the optimal forcing $\hat{\mathbf{f}}_1$ are strong: the input related to $\hat{\mathbf{f}}_1$ therefore may not be neglected, and the ratio $d_u(x_1)/d_u(x_0)$ with $x_0 = 0.3$ and $x_1 = 0.5$ does not yield a fair evaluation of the amplification of the flow, since all inputs are not taken into account.

In the following, after introducing the equation governing the mean perturbation kinetic energy flux (Sect. 4.2.1), we will present a global and a local parameter to assess the instability of an amplifier flow (Sect. 4.2.2). Results are illustrated with the dominant optimal forcing and response at frequency $F = 100$. In Sect. 4.2.3, we will analyze the whole frequency range by discussing the results with respect to the Orr and TS instability mechanisms.

4.2.1 Energetic approach

In order to better characterize the amplification process, we consider the equations governing the mean kinetic energy associated with a harmonic perturbation $\mathbf{u}'$ triggered by a harmonic forcing $\mathbf{f}'$ of frequency ω. By first taking the dot-product of Eq. (3) with $\mathbf{u}'$, then averaging over one period $T = 2\pi/\omega$ and finally integrating in space over an arbitrary domain Ω, we obtain the equation

$$\oint_{\partial\Omega} \left(\overline{k'}\mathbf{U}\cdot\mathbf{n} + \overline{p'\mathbf{u}'}\cdot\mathbf{n} - 2\nu\overline{\mathcal{D}'}\cdot\overline{\mathbf{u}'}\cdot\mathbf{n} \right) \mathrm{d}s = \int_{\Omega} \left(\underbrace{\overline{\mathbf{f}'\cdot\mathbf{u}'}}_{W} \underbrace{-\overline{\mathcal{R}'}:\mathcal{D}}_{P} - \underbrace{2\nu\overline{\mathcal{D}'}:\overline{\mathcal{D}'}}_{D} \right) \mathrm{d}\Omega \tag{19}$$

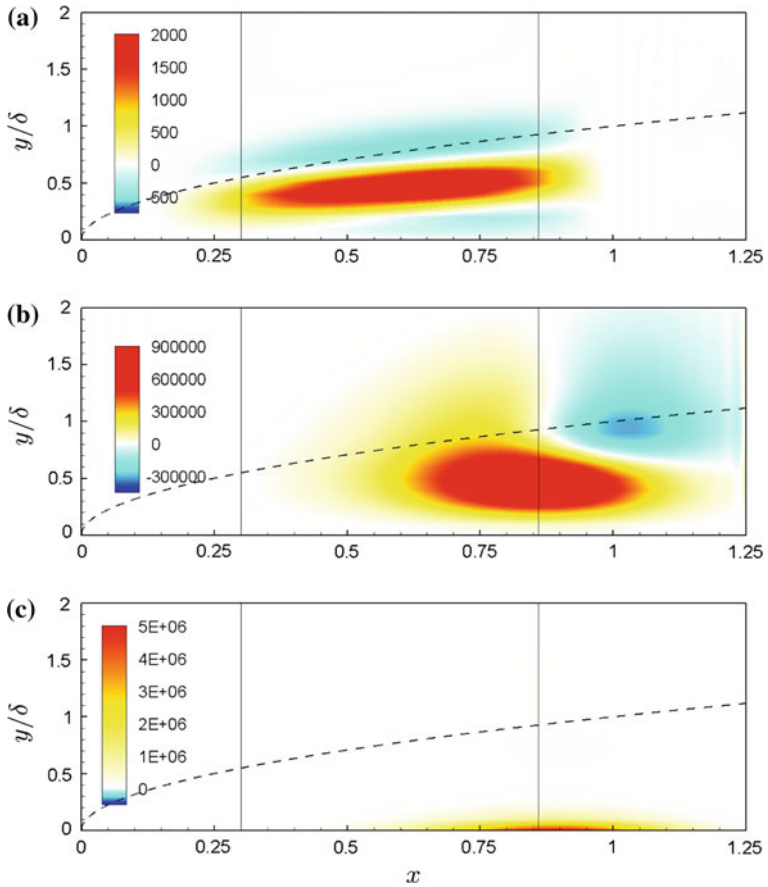

Fig. 5 Source terms of the kinetic energy flux Eq. (19) for the optimal forcing/response at $F = 100$. **a** External power W, **b** production P and **c** dissipation D. The *dashed line* indicates the local displacement thickness $\delta(x)/\delta$ of the boundary layer

where the following notations are used: $\overline{(\cdot)} = T^{-1}\int_0^T (\cdot)\mathrm{d}t$ defines a time average quantity, $k' = (\mathbf{u}' \cdot \mathbf{u}')/2$ is the point-wise perturbation kinetic energy, $\mathbf{n}$ is the outward normal vector to the domain Ω, $\mathcal{D}$ (respectively $\mathcal{D}'$) is the strain rate tensor of the base-flow (respectively perturbation), and $\mathcal{R}'$ is the Reynolds-stress tensor. Since the above equation is written in conservative form, it relates the boundary integral on the left-hand-side to various source terms on the right-hand-side. The boundary integral has three components: the first one is the mean perturbation kinetic energy flux, the second is the mean velocity–pressure correlation, and the last one is the viscous diffusion term. In the present study, we have observed that the first term always dominates the other ones. In the following, we will therefore refer to the boundary integral term as the mean perturbation kinetic energy flux. In the source term appearing in the right-hand-side of Eq. (19), we distinguish again three terms. W is called the external power and expresses the mean power directly supplied by the external force to the perturbation. P is the production term and corresponds to the mean power extracted from the base-flow and transferred to the perturbation. D is the dissipation term and characterizes the mean power lost due to viscous stresses. Since W is the only term directly involving the forcing, it is an extrinsic source. On the other hand, the balance $P - D$ between the production and dissipation terms is an intrinsic source.

The external power W, production P, and dissipation D terms are displayed in Fig. 5a–c in the case of the dominant optimal forcing/response at frequency $F = 100$. The external power W is the lowest term in magnitude. It is either positive or negative, depending on the wall-normal location. The overall integral in space is positive indicating that the forcing globally supplies power to the fluctuations. In the stream-wise direction, the external power is nearly uniformly distributed between branch I and II. This spatial distribution results from the definition of the external power as the product between the optimal forcing $\hat{\mathbf{f}}_1$ and the optimal response $\lambda_1\hat{\mathbf{u}}_1$. The external power displays the strongest value in the overlapping region between the optimal response located near branch II and the optimal forcing located near branch I. This region can be viewed as the one where the external power should be injected to obtain the largest response. It is different from the region

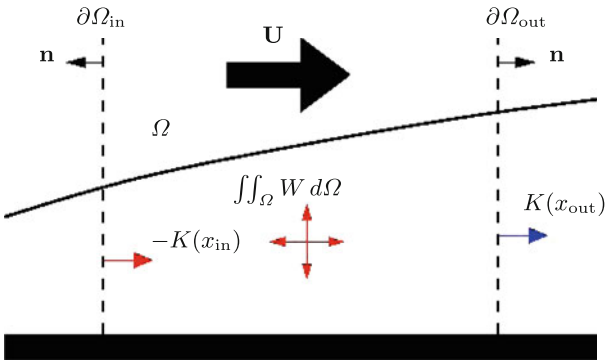

Fig. 6 Spatial domain Ω used to define the amplification parameter Λ. The inlet and outlet boundaries are located at $x_{\rm in}$ and $x_{\rm out}$. The inputs (*red*) consist of the energy flux at the inlet $-K(x_{\rm in})$ and the external power $\iint_\Omega W\,{\rm d}\Omega$. The output (*blue*) is the energy flux at the outlet $K(x_{\rm out})$ (color figure online)

where the forcing displays the strongest amplitudes. This is a typical feature of open flows as discussed by Chomaz [6] and Marquet et al. [7] in the case of globally unstable flows.

The production term P is much stronger in magnitude than the power term W and displays positive values in the whole area comprised within branch I and II. In this region, the mean power is extracted from the base-flow and transferred to the fluctuations. In the stream-wise direction, the production term is largest near branch II since it solely depends on the optimal response $\lambda_1\hat{\mathbf{u}}_1$. In the wall-normal direction, the strongest values are observed below the local displacement thickness of the boundary layer, between the critical layer and the Stokes layer. This is in agreement with the classical interpretation of the Tollmien–Schlichting instabilities [30], based on the positiveness of $-\overline{u'v'}\partial_y U$, the dominant production term in a boundary layer. The viscous effect induces the Reynolds stress term $\overline{u'v'}$ to be strictly negative between the critical layer and the Stokes layer, leading to a strictly positive production term. Finally, the dissipation term D is located very close to the wall near branch II and counterbalances the production term since $-D < 0$.

4.2.2 Global and local amplification parameters

To define an energy-based amplification parameter, we consider the domain Ω shown in Fig. 6, where $\partial\Omega_{\rm in}$ (respectively $\partial\Omega_{\rm out}$) is the inlet (respectively outlet) boundary located at station $x_{\rm in}$ (respectively $x_{\rm out}$). Equation (19) can be rewritten as

$$K(x_{\rm out}) + K(x_{\rm in}) = \int_\Omega W\,{\rm d}\Omega + \int_\Omega (P-D)\,{\rm d}\Omega, \quad K(x) = \int_0^\infty \left(\overline{k'}\mathbf{U}\cdot\mathbf{n} + \overline{p'\mathbf{u}'}\cdot\mathbf{n} - 2\nu\overline{\mathcal{D}'\cdot\mathbf{u}'}\cdot\mathbf{n}\right){\rm d}y \tag{20}$$

For the input–output analysis, the output is defined as the energy flux at the outlet ($K(x_{\rm out})$), while the inputs are the energy flux at the inlet ($-K(x_{\rm in})$) and the external power integrated over the domain Ω ($\int_\Omega W\,{\rm d}\Omega$). The amplification parameter is the ratio between the output and the inputs

$$\Lambda = \frac{K(x_{\rm out})}{-K(x_{\rm in}) + \iint_\Omega W\,{\rm d}\Omega} \tag{21}$$

It is worth noting that this ratio compares two quantities of the same physical dimension, unlike the gain G defined in Eq. (10). Using Eq. (20), the amplification parameter can be rewritten as

$$\Lambda = 1 + \frac{\int_\Omega (P-D)\,{\rm d}\Omega}{-K(x_{\rm in}) + \int_\Omega W\,{\rm d}\Omega} \tag{22}$$

A threshold value for the amplification can now be defined without ambiguity. $\Lambda > 1$ indicates an intrinsic amplification of the energy in the domain because the intrinsic source term $\int_\Omega (P-D)\,{\rm d}\Omega$ is positive, while $\Lambda < 1$ corresponds to a damping. This definition is quite general and depends on the choice of the domain

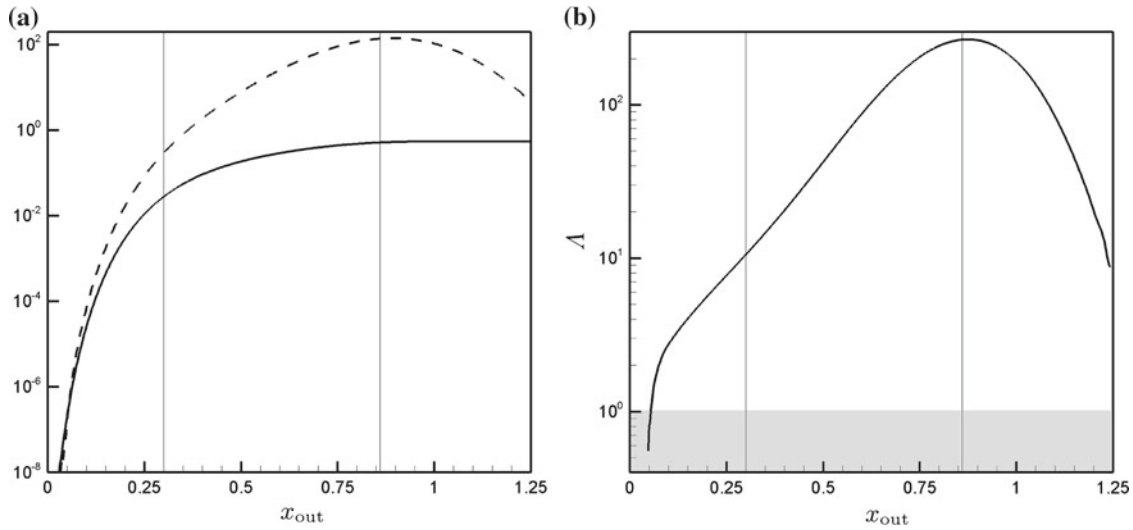

Fig. 7 Global amplification for the optimal singular mode at $F = 100$. **a** Kinetic energy flux $K(x_{\mathrm{out}})$ (*dashed line*) and external power $\iint_{\Omega} W \, \mathrm{d}\Omega$ (*solid line*) as a function of the outlet location x_{out}. **b** Global amplification parameter Λ as a function of x_{out}. The *vertical lines* delimit the convectively unstable region. The *gray area* emphasizes the threshold amplification $\Lambda = 1$

Ω. Note that, if we choose a domain that does not contain any external forcing, the external power vanishes. The amplification parameter would then be defined as $K(x_{\mathrm{out}})/(-K(x_{\mathrm{in}}))$, which recovers the amplification parameter $d_u(x_1)/d_u(x_0)$ discussed at the beginning of Sect. 4.2.

In the following, we will try to give a detailed analysis of the amplification process by considering both a global amplification parameter and a local one. The global amplification parameter is built by choosing the inlet boundary $\partial\Omega_{\mathrm{in}}$ as the inlet boundary of the computational domain ($x_{\mathrm{in}} = -0.5$) and by varying the outlet boundary location x_{out}. In the specific case $x_{\mathrm{out}} = 1$, Ω corresponds to the optimization domain used in Sect. 3. Since the perturbation energy flux vanishes at the inlet, the global amplification parameter reads

$$\Lambda(x_{\mathrm{out}}) = \frac{K(x_{\mathrm{out}})}{\iint_{\Omega} W \, \mathrm{d}\Omega} = 1 + \frac{\int_{\Omega} (P - D) \, \mathrm{d}\Omega}{\int_{\Omega} W \, \mathrm{d}\Omega} \tag{23}$$

This global amplification parameter is used for quantifying the amplification of the optimal forcing/response at $F = 100$. The energy flux (dashed line) and external power (solid line) are depicted in Fig. 7a as a function of x_{out}. The global amplification parameter is shown in Fig. 7b, where the gray color highlights the region $\Lambda < 1$. The global amplification parameter is above 1 for almost every position of the outlet boundary. Amplification is observed upstream of branch I: the amplification parameter Λ is greater than 1 for values of x_{out} above 0.05 and reaches a value of 10 at branch I. As the amplification within this region can only be due to the Orr mechanism, this value yields a quantification of the perturbation kinetic energy flux extracted by this mechanism. In the locally unstable region, the amplification increases from $\Lambda \approx 10$ to $\Lambda = 268$ that is reached at $x_{\mathrm{out}}^{\mathrm{max}} = 0.87$, slightly downstream of branch II. Further downstream, the amplification decreases to reach $\Lambda \approx 70$ when the domain corresponds to the optimization domain ($x_{\mathrm{out}} = 1$). This decrease is clearly associated with a local damping of the energy flux.

A local amplification parameter can be defined to better characterize the region displaying local amplification. We consider a small domain Ω in the stream-wise direction, defined by $x_{\mathrm{in}} = x$ and $x_{\mathrm{out}} = x + \mathrm{d}x$. Taking the limit $\mathrm{d}x \to 0$ in Eq. (22), we obtain

$$\gamma = \frac{1}{\gamma_{\mathrm{ext}}} \frac{\mathrm{d}K}{\mathrm{d}x} = 1 + \frac{\gamma_{\mathrm{int}}(x)}{\gamma_{\mathrm{ext}}(x)} \quad , \quad \gamma_{\mathrm{ext}}(x) = \int_0^{\infty} W(x, y) \mathrm{d}y \quad , \quad \gamma_{\mathrm{int}}(x) = \int_0^{\infty} (P(x, y) - D(x, y)) \mathrm{d}y \tag{24}$$

where γ_{ext} and γ_{int} are the extrinsic and intrinsic local sources. Figure 8a displays these quantities as a function of the location x for the optimal forcing/response at $F = 100$. The extrinsic local source is maximum in the middle of the locally unstable region, while the intrinsic local source is strongest slightly upstream of branch II. For every location, the intrinsic source is much larger than the extrinsic source. The local amplification

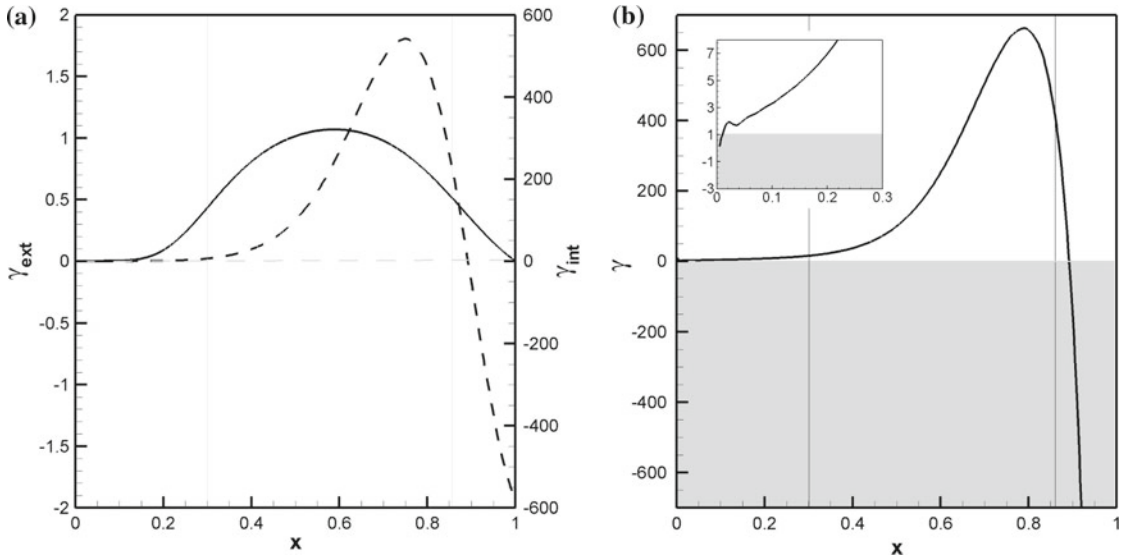

Fig. 8 Local amplification for the optimal singular mode at $F = 100$. **a** Local amplification of the kinetic energy flux as a function of the stream-wise coordinate x. The *solid* and *dashed lines* stand for the extrinsic γ_{ext} and intrinsic γ_{int} local sources respectively. **b** Location amplification parameter γ as a function of x. *Close-up view* of the region upstream of the convectively unstable region which is delimited in both figures by the *vertical lines*

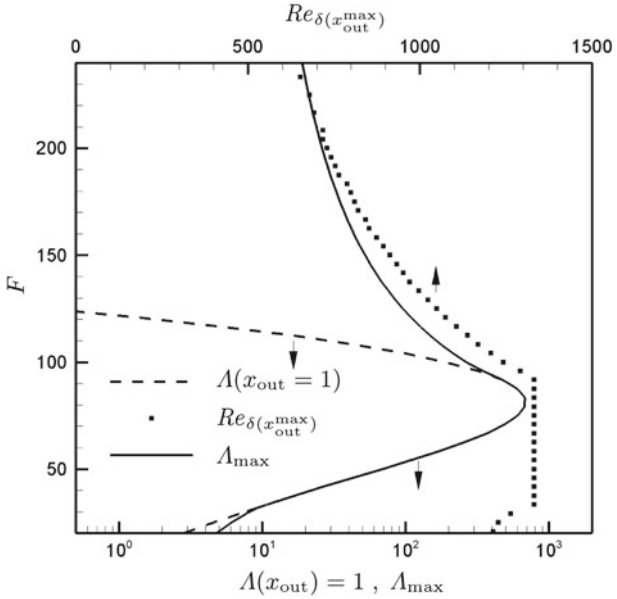

Fig. 9 Global amplification as a function of the frequency F. The *dashed line* represents the global amplification $\Lambda(x_{\text{out}} = 1)$. The *solid line* designates the maximum value of the global amplification parameter $\Lambda_{\max} = \max_{x_{\text{out}} \leq 1} \Lambda(x_{\text{out}})$. The *symbols* are the local Reynolds numbers $Re_{\delta(x_{\text{out}}^{\max})}$ at the location $x_{\text{out}}^{\max}$ where the maximum is obtained. The *arrows* in the figure indicate which axis to consider for each curve

parameter is shown in Fig. 8b. It is above 1 for every location x indicating that the local amplification is intrinsic. This intrinsic local amplification is much stronger for the Tollmien–Schlichting mechanism than for the Orr mechanism.

4.2.3 Global amplification parameter as a function of frequency

The analyzes led for $F = 100$ in the case of local and global amplification parameters can be repeated for other frequencies. Figure 9 offers a synthetic view of the global amplification parameter Λ over all frequencies.

We first focus on the dashed line that corresponds to $\Lambda(x_{\text{out}} = 1)$, for which the outlet boundary is fixed to the outlet of the optimization domain. Maximal amplification is obtained for the frequency $F = 83$ where $\Lambda(x_{\text{out}} = 1) \approx 680$. For higher frequencies $F > 120$, there is no global amplification since $\Lambda(x_{\text{out}} = 1) < 1$. Indeed, as the frequency increases, the convectively unstable region moves upstream and the perturbations are damped out between branch II and the outlet $x_{\text{out}} = 1$. This damping is mainly related to the negative values of the production term that arise downstream of branch II (see Fig. 5b). For lower frequencies, the global amplification parameter is decreasing with frequency due to the fact that the convectively unstable region progressively moves downstream and therefore out of the optimization domain (see discussion at the end of Sect. 3.2). Some complementary insight may be gained by considering a domain whose outlet is adapted to get the maximum value of the amplification parameter:

$$\Lambda_{\max}(F) = \max_{x_{\text{out}} \leq 1} \Lambda(x_{\text{out}}, F) \tag{25}$$

The specific value of the outlet location where the maximum is reached is denoted by $x_{\text{out}}^{\max}$. The local displacement thickness Reynolds number based on this outlet location is denoted $Re_{\delta(x_{\text{out}}^{\max})}$. Results for $\Lambda_{\max}(F)$ and $Re_{\delta(x_{\text{out}}^{\max})}$ are respectively shown by the solid line and the symbols in Fig. 9. Comparison with the purple curve in Fig. 3c shows that the maximal amplification parameter $\Lambda_{\max}$ is obtained when the half-plane Ω is chosen to extend up to branch II. For the present region of interest $Re_x < Re$ $(x \leq 1)$, the maximum values of $\Lambda_{\max}$ are obtained when x_{out} is located at the downstream border of the optimization domain $x = 1$ and for frequencies F around 83. The maximum values of the curve $\Lambda_{\max}(F)$ are therefore the same as those obtained for $\Lambda(x_{\text{out}} = 1)(F)$. For $F > 100$, the maximal values $\Lambda_{\max}$ are obtained for outlet locations inside the optimization domain $x_{\text{out}} < 1$. The strong discrepancy observed between the solid and dashed lines shows that there is a damping of the energy flux in the region $x_{\text{out}}^{\max} \leq x \leq 1$, which has already been mentioned above. For very high values of the frequency, $F \approx 230$, it is seen that the amplification parameter is still superior to 1 with a value around $\Lambda_{\max} \approx 20$. As the flow is stable to Tollmien–Schlichting waves at such high frequencies, only the Orr mechanism and non-parallel effects [29] may be responsible for this amplification.

5 Conclusion

In this paper, from a numerical point of view, we have introduced a new method to compute the largest singular values of the global resolvent. The method follows the "discretize-then-optimize" scheme and allows to consider different measures for the forcing space and the response space. Also, the use of an iterative Arnoldi approach enables to compute sub-optimals.

From a physical point of view, we have analyzed the singular vectors for a flow developing over a sharp-leading-edge flat plate. It was shown that the optimal forcings are located near branch I while the optimal responses are near branch II. The downstream evolution of the energy density of the optimal response compares favorably with the local e^N method, except in the region where the optimal forcing is strong. To gain some new insight about the spatial growth of the energy density, we introduced an energetic input–output approach, which showed that this growth was solely due to intrinsic amplifying mechanisms related to the Orr and Tollmien–Schlichting mechanisms and not to the externally supplied power by the optimal forcing. It was also shown how to quantify the amplifying behavior of the dominant optimal response $\hat{\mathbf{u}}_1$, by considering an amplification parameter Λ comparing a mean-fluctuating kinetic energy flux of the optimal response with the externally supplied mean power by the optimal forcing. This yields for each frequency the "true" potential of amplification of the flow. It has been shown in particular that the Orr mechanism remains active at very high frequencies.

From a broader perspective, we have shown that amplifier flows should be characterized in the global framework by analyzing the singular values and vectors of the flow (and not the eigenvalues of the Jacobian). We think that this approach is conceptually simple because it is based on the singular value decomposition of the global resolvent, which is a robust and very general concept. It also yields a direct link with receptivity studies since the spatial location of the optimal forcings identifies sensitive regions of the flow. In the case of weakly-non-parallel flows as boundary layers or jets, such an analysis compares well with the traditional local e^N method. This is important, since a general concept has to encompass particular cases. The global approach is comparatively much more intensive from a computational point of view, which strongly favors the cheap local approaches (even though these local approaches may be technically and conceptually much more involved). On the other hand, for amplifier flows violating the weakly-non-parallel assumption, the singular values/vectors approach is the only possibility.

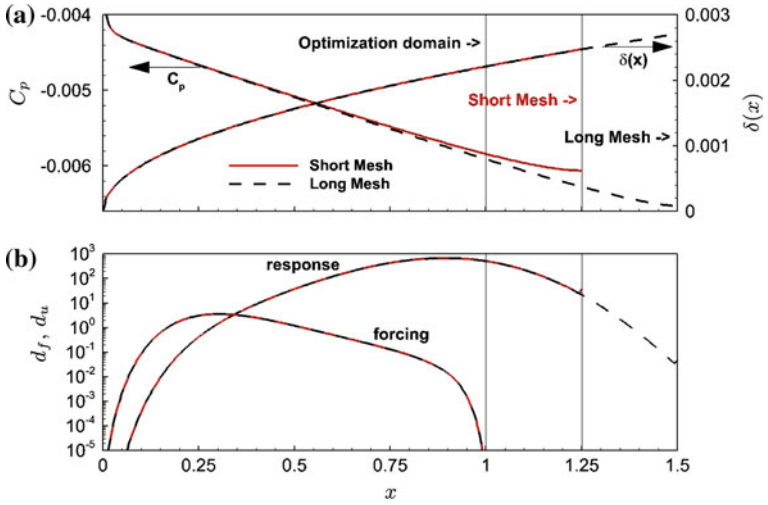

Fig. 10 $Re = 6 \times 10^5$. Comparison of results obtained on a short- (*red solid lines*) and a long mesh (*black dashed line*) extending respectively up to $x = 1.25$ and $x = 1.5$. The optimization domain has been kept constant ($x \leq 1$). **a** Pressure coefficient and displacement boundary-layer thickness of the base-flow as a function of x. **b** Stream-wise evolution of energy density functions of dominant optimal forcing $\hat{\mathbf{f}}_1$ and response $\lambda_1 \hat{\mathbf{u}}_1$ (color figure online)

Appendix: Influence of downstream boundary condition

We check in this section that the outflow boundary condition imposed at $x = 1.25$ does only have a minor influence on the results within the region of interest (which extends up to $x = 1$). For this, we achieve computations with a mesh extending up to $x = 1.5$, while keeping the optimization domain within $x \leq 1$. In Fig. 10a, we compare the stream-wise evolution on the flat plate of the pressure coefficient C_p and of the displacement boundary-layer thickness $\delta(x)$ for the short and long meshes (which respectively extend up to $x = 1.25$ and $x = 1.5$). A slight mismatch is observed for the pressure coefficient, but the associated pressure gradient discrepancy is extremely weak and has no influence on the boundary-layer displacement thickness evolution and on the friction coefficient (not shown here). In Fig. 10b, we have plotted the stream-wise evolution of the energy density functions associated with $\hat{\mathbf{f}}_1$ and $\lambda_1 \hat{\mathbf{u}}_1$ for $F = 100$. We observe that the curves for the long mesh coincide with those of the short mesh nearly perfectly for $x \leq 1$.

References

1. Huerre, P., Rossi, M. : Hydrodynamic instabilities in open flows. In: Godrèche, C., Manneville, P. (eds.) Hydrodynamics and Nonlinear Instabilities, pp. 81–294. Cambridge University Press, Cambridge, UK (1998)
2. Zebib, A.: Stability of a viscous flow past a circular cylinder. J. Eng. Math. **21**(2), 155–165 (1987)
3. Jackson, C.P.: A finite-element study of the onset of vortex shedding in flow past variously-shaped bodies. J. Fluid Mech. **182**, 23–45 (1987)
4. Provansal, M., Mathis, C., Boyer, L.: Benard-Von Karman instability—transient and forced regimes. J. Fluid Mech. **182**, 1–22 (1987)
5. Sipp, D., Lebedev, A.: Global stability of base and mean flows: a general approach and its applications to cylinder and open cavity flows. J. Fluid Mech. **593**, 333–358 (2007). doi:10.1017/S0022112007008907
6. Chomaz, J.M.: Global instabilities in spatially developing flows: non-normality and nonlinearity. Ann. Rev. Fluid Mech. **37**, 357 (2005)
7. Marquet, O., Lombardi, M., Chomaz, J.M., Sipp, D., Jacquin, L.: Direct and adjoint global modes of a recirculation bubble: lift-up and convective non-normalities. J. Fluid Mech. **622**, 1–21 (2009)
8. Trefethen, L.N., Trefethen, A.E., Reddy, S.C., Driscoll, T.A.: Hydrodynamic stability without eigenvalues. Science **261**(5121), 578–584 (1993)
9. Schmid, P.J.: Nonmodal stability theory. Ann. Rev. Fluid Mech. **39**, 129–162 (2007)
10. Marquet, O., Sipp, D., Chomaz, J.M., Jacquin, L.: Amplifier and resonator dynamics of a low-Reynolds-number recirculation bubble in a global framework. J. Fluid Mech. **605**, 429 (2008)
11. Blackburn, H.M., Barkley, D., Sherwin, S.J.: Convective instability and transient growth in flow over a backward-facing step. J. Fluid Mech. **603**, 271 (2008)
12. Cantwell, C.D., Barkley, D.: Computational study of subcritical response in flow past a circular cylinder. Phys. Rev. E **82**(2, part 2), 026315 (2010)

13. Cantwell, C.D., Barkley, D., Blackburn, H.M.: Transient growth analysis of flow through a sudden expansion in a circular pipe. Phys. Fluids **22**(3), 034101 (2010)
14. Schmid, P.J.: Dynamic mode decomposition of numerical and experimental data. J. Fluid Mech. **656**, 5–28 (2010)
15. Farrell, B., Ioannou, P.: Optimal excitation of three-dimensional perturbations perturbations in viscous constant shear-flow. Phys. Fluids A **5**(6), 2600 (1993)
16. Alizard, F., Robinet, J.C.: Spatially convective global modes in a boundary layer. Phys. Fluids **19**(11), 114105 (2007)
17. Akervik, E., Ehrenstein, U., Gallaire, F., Henningson, D.S.: Global two-dimensional stability measures of the flat plate boundary-layer flow. Eur. J. Mech. B-Fluids **27**(5), 501 (2008)
18. Alizard, F., Cherubini, S., Robinet, J.C.: Sensitivity and optimal forcing response in separated boundary layer flows. Phys. Fluids **21**(6), 064108 (2009)
19. Sipp, D., Marquet, O., Meliga, O., Barbagallo, A.: Dynamics and control of global instabilities in open flows: a linearized approach. Appl. Mech. Rev. **63**, 030801 (2010)
20. Monokrousos, A., Akervik, E., Brandt, L., Henningson, D.: Global three-dimensional optimal disturbances in the blasius boundary-layer flow using time-steppers. J. Fluid Mech. **650**, 181 (2010)
21. Ehrenstein, U., Gallaire, F.: On two-dimensional temporal modes in spatially evolving open flows: the flat-plate boundary layer. J. Fluid Mech. **536**, 209 (2005)
22. Farrell, B.: Optimal excitation of perturbations in viscous shear-flow. Phys. Fluids **31**(8), 2093–2102 (1988)
23. Lopez, J., Marques, F., Rubio, A., Avila, M.: Crossflow instability of finite bödewadt flows: transients and spiral waves. Phys. Fluids **21**, 114107 (2009)
24. Do, Y., Lopez, J., Marques, F.: Optimal harmonic response in a confined bödewadt boundary layer flow. Phys. Rev. E **82**, 036301 (2010)
25. Bewley, T.R.: Flow control: new challenges for a new renaissance. Prog. Aerosp. Sci. **37**(1), 21–58 (2001)
26. Jiménez, J.: Localized amplification of energy in turbulent channels. Center for Turbulence Research, Annual Research Briefs (2009)
27. Lehoucq, R.B., Sorensen, D.C.: Deflation techniques for an implicitly restarted Arnoldi iteration. SIAM J. Matrix Anal. Appl. **17**(4), 789–821 (1996)
28. Amestoy, P.R., Duff, I.S., Koster, J., L'Excellent, J.Y.: A fully asynchronous multifrontal solver using distributed dynamic scheduling. SIAM J. Matrix Anal. Appl. **23**(1), 15–41 (2001)
29. Gaster, M.: On the effects of boundary-layer growth on flow stability. J. Fluid Mech. **66**, 465–480 (1974)
30. Drazin, P., Reid, W.: Hydrodynamic Stability. Cambridge University Press, Cambridge, UK (2004)